

Spatial Distribution of γ -Crystals in Metallocene-Made Isotactic Polypropylene Crystallized under Combined Thermal and Flow Fields

Yan Wang,[†] Ji-Lin Pan,[†] Yimin Mao,[‡] Zhong-Ming Li,^{*,†} Liangbin Li,[§] and Benjamin S. Hsiao^{*,‡}

College of Polymer Science and Engineering and State Key Laboratory of Polymer Materials Engineering, Sichuan University, Chengdu 610065, China, Department of Chemistry, Stony Brook University, Stony Brook, New York 11794-3400, and National Synchrotron Radiation Laboratory and Department of Polymer Science and Engineering, University of Science and Technology of China, Hefei 230026, China

Received: January 11, 2010; Revised Manuscript Received: April 19, 2010

The present Article reports the relationships between molecular orientation, formation, and spatial distribution of γ -crystals in metallocene-made isotactic polypropylene (m-iPP) samples prepared by two industrial processes: conventional injection molding (CIM) and oscillatory shear injection molding (OSIM), in which combined thermal and flow fields typically exist. In particular, spatial distributions of crystallinity, fraction of γ -crystal (f_γ) with respect to α -crystal, and lamella-branched shish-kebab structure in the shaped samples were characterized by synchrotron two-dimensional (2D) wide-angle X-ray diffraction (WAXD) and small-angle X-ray scattering (SAXS) techniques. The results showed that the crystallinity in any given region of OSIM samples was always higher than that of CIM samples. The value of f_γ increased monotonously from skin to core in CIM samples, whereas the corresponding f_γ increased nonmonotonically in OSIM samples. The spatial distribution of γ -crystal in OSIM samples can be explained by the epitaxial arrangement between γ - and α -crystal in a lamella-branched shish-kebab structure. In the proposed model, the parent lamellae of α -crystal provide secondary nucleation sites for daughter lamellae of α -crystal and γ -crystal, and the different content of parent lamellae results in varying amounts of γ -crystal. In OSIM samples, the smallest parent–daughter ratio ($[R] = 1.38$) in the core region led to the lowest fraction of γ -crystal (0.57), but relatively higher γ -crystal content (0.69) at 600 and 1200 μm depth of the samples (corresponding to $[R]$ of 4.5 and 5.8, respectively). This is consistent with the proposed model where more parent lamellae provide more nucleation sites for crystallization, thus resulting in higher content of γ -crystal. The melting behavior of CIM and OSIM samples was studied by differential scanning calorimetry (DSC). The observed double-melting peaks could be explained by the melting of γ - and α -crystal of the shaped samples. The f_γ distribution calculated from the relative areas of the peaks in the DSC scans was also consistent with the WAXD results.

Introduction

Metallocene-made isotactic polypropylene (m-iPP) and its copolymers have gained popularity in industry. For example, highly transparent m-iPP parts can be made by injection molding, which becomes a potential alternative of highly transparent amorphous products such as polystyrene (PS). Melt spun m-iPP fibers exhibit higher strength, better uniformity, and better anti-infiltration than Ziegler–Natta iPP (ZN-iPP) fibers. Packaging films based on m-iPP also exhibit desirable low-temperature toughness. The unique properties of m-iPP are closely related to the structure and morphology; thus formation and control of the structures in these materials are important both technologically and scientifically.

It is well-known that m-iPP has crystalline characteristics that are quite different from those of traditional ZN-iPP.¹ Traditional iPP generally crystallizes in stable α -crystal, while m-iPP has the tendency to crystallize into γ -crystal (e.g., at atmospheric pressure and for high molecular weight samples).^{2–8} The γ -crystal of PP crystals has an orthorhombic structure and has

been recognized a few decades ago.^{9–11} The chain in γ -crystal is in the stable 3-fold helical conformation, the same as those in α - and β -crystals. Unlike α - and β -crystals, the chain axes of which are parallel in the crystals, the γ -crystal is peculiar, in which the direction of the chain axis in adjacent bilayers is tilted by about 80° against each other and by about 40° with respect to the b -axis. The different polymorphic behavior of iPP samples prepared with heterogeneous (Ziegler–Natta made) and homogeneous (metallocene made) catalysts is due to the different type and distribution of insertion mistakes during polymerization along the chains (i.e., stereodefects and regiodefects). Because the distribution of defects in the chains of m-iPP is random in nature, even a small amount of defects can significantly reduce the length of the regular isotactic sequences and result in higher content of γ -phase crystals.^{2,5–8} In contrast, for ZN-iPP, the majority of the defects may be segregated in a small fraction of chain segments that are difficult to crystallize, so that much longer, fully isotactic sequences can be produced, leading to dominant crystallization of the α -crystal.¹

Besides the aforementioned effect of shortening the regular isotactic sequences, it is still not completely clear how the environmental conditions influence the γ -crystal formation in m-iPP, especially under applied stress. One aspect of the information is clear; that is, the γ -crystal is thermodynamically

* To whom correspondence should be addressed. E-mail: zmli@scu.edu.cn (Z.-M.L.), bhsiao@notes.cc.sunysb.edu (B.S.H.).

[†] Sichuan University.

[‡] Stony Brook University.

[§] University of Science and Technology of China.

avored in m-iPP.^{2,8,12} This is because a high amount of γ -crystal always develops in m-iPP under the slow isothermal crystallization at high temperatures,^{2,8} or at low cooling rate under nonisothermal crystallization conditions.¹² The impact of pressure on the γ -crystal crystallization has also been reported recently.¹³ With the increase in pressure, the γ -crystal begins to coexist with the α -crystal, and it becomes the dominant structure at high pressures (e.g., 2000 bar). The present work focuses on the formation of γ -crystal in m-iPP under combined shear and thermal fields existing in injection molding. Of particular interest is to clarify the role of the temperature gradient and molecular orientation. The understanding of γ -crystal formation in m-iPP under deformation is an interesting subject because during injection molding the molten chains shall align parallel to the flow direction, which appears nonfavorable to the unique nonparallel chain arrangement of the γ -crystal.

Typical processing of polymers usually involves applications of stress field, which inevitably affect orientation of polymer chain, its ability to form primary nuclei, and resulting morphology. Thus, the relationship between flow field and polymer crystallization is an important subject that has drawn considerable interest from many research groups.^{14–20} It is widely accepted that the sheared polymer melt exhibits an enhanced rate of crystallization and different morphology when compared to those in the quiescent melt. Among the different morphologies formed during shear-induced crystallization of polymer melts, the shish-kebab structure has been recognized as a dominant feature, which directly affects mechanical properties.^{21,22} In injection-molded iPP samples, the shear zone between skin and core regions can generally be characterized by a “shish-kebab” structure.^{23–26} In this structure, kebabs are comprised of folded chain crystals with the *c*-axis aligned preferentially along the flow direction, whereas the daughter lamellae are also found with their *a**-axes parallel to the *c*-axes of parent lamellae (or shish) or flow direction.^{26–28}

The influence of shear stress on the formation of γ -crystal in iPP has been reported in the literature. For example, Hsiao et al. investigated the effect of shear flow on the γ -crystal formation in long-chain branched isotactic polypropylene (LCB-iPP). They concluded that the higher content of γ -crystal formed in LCB-iPP than that in linear iPP under shear could be mainly attributed to the regio-defect of polymer chains.²⁹ Hong and Seo studied a polypropylene-containing terpolymer prepared by Ziegler–Natta catalyst under a mixed elongational and shear flows in the foaming process. They concluded that the high expansion ratio is a necessary condition for the creation of higher γ -crystal content.³⁰ In the current study, we are interested in understanding the role of shear field in the formation of γ -crystal in m-iPP. Some particular questions are as follows: (1) Is γ -crystal a thermodynamically favored crystal in the oriented melt of m-iPP? (2) How does the degree of molecular orientation affect the formation of crystalline structure in m-iPP, especially γ -crystal? (3) Can we describe the γ -crystal spatial distribution in m-iPP under complex temperature and flow field conditions typically encountered in industrial polymer processing? These issues are very important in both academic and application studies, but they have not been systematically investigated.

In this study, we begin to address the above questions by examining m-iPP samples obtained through both conventional injection molding (CIM) and oscillatory shear injection molding (OSIM) processes. The primary feature of OSIM is that the hot melt in the mold is subjected to high oscillatory shear stress, given by two pistons moved reversibly at the same frequency, where the effect of flow field can be examined. OSIM has been

proved to be an effective means to control the structure and morphology of polymers through flow-induced orientation. Two-dimensional (2D) synchrotron wide-angle X-ray diffraction (WAXD) and small-angle X-ray scattering (SAXS) were used to characterize the morphological distribution in m-iPP samples and to determine the effects of flow and temperature on crystallization. The results indicate that the thermodynamically favored γ -crystal (in the quiescent state) seems to be unstable under strong shear field. Some insights into this subject were obtained and discussed.

Experimental Section

Materials. The chosen isotactic polypropylene (iPP), made by metallocene catalysis, was supplied by the Basel Co. The molecular weight of iPP was determined by gel permeation chromatography (GPC) in 1,2,4-trichlorobenzene at 160 °C. The average weight molecular weight M_w and the molecular weight distribution were 407 000 and 2.25, respectively. The melt flow index (MFI) of the chosen iPP was 12 g/10 min (at 190 °C and with 2.16 kg of weight). The ¹³C NMR spectra of the sample were recorded on a Bruker AVANCE 400 operating at 50 MHz in the Fourier transform mode of 10% w/v polymer solutions in deuterated 1,2,4-trichlorobenzene and benzene at 120 °C. No or negligible regioerrors (2,1 insertions) could be observed in the ¹³C NMR spectra of the samples. [mr]% and [rr]% are 3.09 and 0.86, respectively, and [mm]% is 96.05.

Preparation of CIM and OSIM Samples. The material was first melt-injected into a dumbbell mold of the injection molding machine with a temperature profile of 170–200 °C from hopper to nozzle. Subsequently, OSIM technology was applied with oscillation shear frequency of 0.3 Hz under the pressure of 120 bar and molding temperature of 110 °C. The detailed description of OSIM technology has been reported previously.³¹ The main feature of OSIM is as follows: the continuous oscillatory shear was provided at the packing stage of the injection molding cycle. When the movements of two pistons were out of phase with each other during the holding period, the resulting oscillatory shear force would shape the iPP melt reciprocally along the length direction of the mold. Before solidifying, the iPP melt continuously underwent repeated shear stress until the pistons were stopped. CIM was also carried out under the same processing conditions (only without oscillatory shear) for comparison.

Crystal Structure Characterization by WAXD and SAXS.

Two-dimensional (2D) wide-angle X-ray diffraction (WAXD) was used to characterize the crystalline structure and molecular orientation distribution along the sample depth direction. 2D WAXD patterns were collected in a scattering beamline at the National Synchrotron Radiation Laboratory, China. The chosen X-ray wavelength λ was 1.54 Å, where the sample to detector distance was 295 mm. A MAR 345 image plate detector (by MAR Research Co. Ltd., Germany) was used to collect all WAXD images. The sample was machined from the central part of a dumbbell bar (as shown in Figure 1, thickness was 4 mm) into a thin film with thickness of 1 mm and width of 6 mm. The WAXD measurements were taken at 100, 600, 1200, 1800, 2400, 3000 μ m, respectively, from the surface along the TD direction as shown in Figure 1 (only one-half-width of each specimen was evaluated; i.e., we assumed the morphological distribution is symmetrical in the central part of the dumbbell sample). The synchrotron illumination spot size was about 0.1 \times 2 mm²; thus the examined position on the sample did not

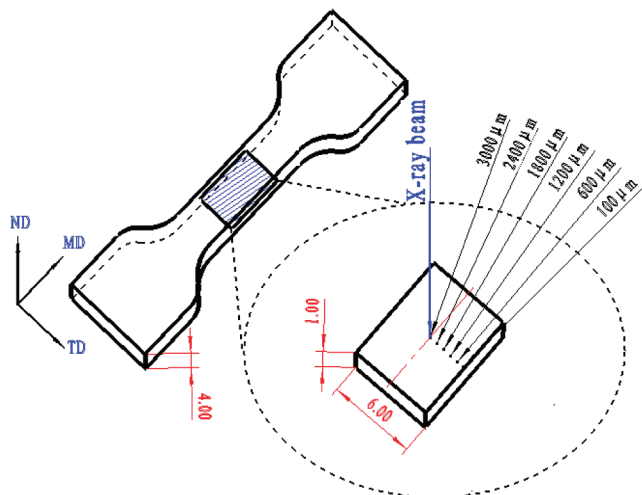


Figure 1. Schematic diagram of the positions of the samples for 2D WAXD and SAXS measurements (MD, the molding direction (i.e., flow direction); TD, the transverse direction; ND, the direction normal to the MD-TD plane). The numbers (100, 600...3000 in μm) represent the distance away from the sample surface along the TD direction.

overlap. The X-ray image without the specimen was also recorded as a background to enable the correction of measured patterns.

To elucidate the depth dependence of molecular orientation along the TD direction, a quantitative measurement was carried out using the Hermans' orientation function defined as follows:

$$f_H = \frac{3\langle \cos^2 \varphi \rangle - 1}{2} \quad (1)$$

where $\cos^2 \varphi$ is the orientation factor defined as

$$\langle \cos^2 \varphi \rangle = \frac{\int_0^{\pi/2} I(\varphi) \cos^2 \varphi \sin \varphi \, d\varphi}{\int_0^{\pi/2} I(\varphi) \sin \varphi \, d\varphi} \quad (2)$$

where φ is the angle between the normal of a given (hkl) crystal plane and shear flow direction, and $I(\varphi)$ is the intensity. The orientation function $f_H = 1$ when the probed axis is perfectly parallel to the reference direction, $f_H = -0.5$ when the probed axis is perfectly perpendicular to the reference direction, and $f_H = 0$ when the probed axis is randomly distributed. The orientation parameter of CIM and OSIM samples was calculated mathematically using Picken's method³² from $2\theta = 17^\circ$ (i.e., 040 and 008 reflections) of WAXD.

Two-dimensional (2D) small-angle X-ray scattering (SAXS) measurements were carried out at the Advanced Polymers Beamline (X27C, $\lambda = 1.371 \text{ \AA}$) in the National Synchrotron Light Source (NSLS), Brookhaven National Laboratory (BNL). A 2D MAR CCD X-ray detector with a resolution of 512×512 pixels (pixel size = $158 \mu\text{m}$) was employed for the SAXS detection. The sample to detector distance was 1755.5 mm. The same as for WAXD measurements, the illuminated zone was changed with the depth of sample as shown in Figure 1.

Differential Scanning Calorimetry (DSC). The DSC measurements were performed with a (DSC) Mettler-Toledo differential scanning calorimeter (model DSC-1) at scan rates of $10^\circ\text{C}/\text{min}$ with 5–6 mg of sample under a flowing nitrogen atmosphere. In accordance with the order from the surface to

core (along the TD direction), the sample was cut using a knife corresponding to the position of 2D WAXD and SAXS measurements.

Results

Crystalline Structures Distribution in CIM and OSIM Samples.

Figure 2 shows 2D WAXD patterns at different depths (i.e., distances from the surface on the machined sample in Figure 1 along the TD direction) of CIM and OSIM samples. At a given depth, the reflections of OSIM samples show a much stronger azimuthal dependence than those of CIM samples, indicating a higher degree of molecular orientation. Meanwhile, the most characteristic diffractions of α - and γ -form, corresponding to $(130)_\alpha$ and $(117)_\gamma$ reflections, appear at different depths of the samples. Figure 3 shows integrated WAXD profiles from different depths in the CIM and OSIM samples (the integration was carried out circularly from the 2D WAXD image). In Figure 3a, it is seen that the main reflection peaks correspond to the coexistence of α - and γ -crystal because they overlap against each other. The most intense diffraction peaks of the α -crystal occur at $2\theta = 14.2^\circ, 17.1^\circ, 18.6^\circ, 21.1^\circ$, and 21.8° , corresponding to $(110)_\alpha$, $(040)_\alpha$, $(130)_\alpha$, $(111)_\alpha$, $(31)_\alpha + (041)_\alpha$, and $(041)_\alpha$ reflections, respectively.³³ The most characteristic diffraction peaks of the γ -crystal occur at $2\theta = 13.8^\circ, 16.7^\circ, 20.1^\circ, 21.2^\circ$, and 21.9° , which can be assigned to $(111)_\gamma$, $(008)_\gamma$, $(117)_\gamma$, $(202)_\gamma$, and $(026)_\gamma$ reflections, respectively.⁹ Therefore, the only remarkable difference in the diffraction patterns of α - and γ -crystals is the third strong peak, which appears at $2\theta = 18.6^\circ$ (i.e., $(130)_\alpha$ reflection) for the α -crystal, and the fourth strong peak at $2\theta = 20.1^\circ$ (i.e., $(117)_\gamma$ reflection) for the γ -crystal (Figures 2 and 3).

An iterative peak-fit procedure was used to describe the amorphous and crystal peaks; thereby, the peak parameters (i.e., height, width, and area) of each crystal reflection were obtained. The area of each peak (corresponding to each reflection) and of the amorphous background curve could be extracted, allowing the estimate of overall crystallinity, X_c .

$$X_c = \frac{\sum A_{\text{cryst}}}{\sum A_{\text{cryst}} + \sum A_{\text{amorp}}} \quad (3)$$

where A_{cryst} and A_{amorp} are the fitted areas of the crystal and amorphous phases. The estimated crystallinity data are shown in Table 1. The crystallinity of the OSIM sample is consistently higher than that of the CIM sample. This is because the higher level of shear flow results in a higher degree of overall crystallinity. It is well-known that, after polymeric fluids are subjected to flow, the polymer chains are oriented and stretched. The stronger is the flow, the easier the molecules are aligned and form crystals due to the reduction of entropy.

The relative content of γ -crystal in our samples was measured as suggested by Turner-Jones et al.:³⁴

$$f_\gamma = I_\gamma(117)/[I_\gamma(117) + I_\alpha(130)] \quad (4)$$

where $I_\gamma(117)$ and $I_\alpha(130)$ represent the fitted areas of the corresponding diffraction peaks above the diffuse halo. Figure 4 shows the distribution of f_γ through the depths of m-iPP samples.

In the case of CIM, f_γ is small (0.57) at $100 \mu\text{m}$ near the surface, then increases gradually toward the core, showing the maximum value (0.74) at $1800 \mu\text{m}$, and staying almost constant

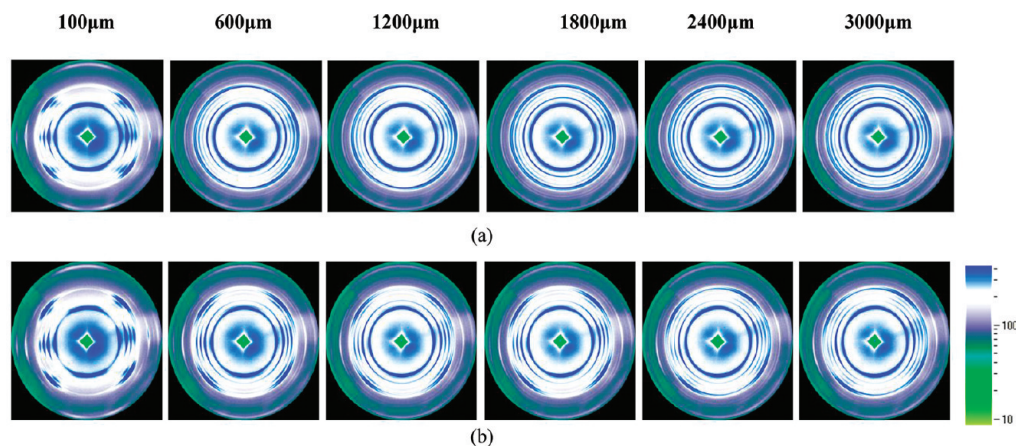


Figure 2. 2D WAXD images at different distances from the surface of (a) CIM and (b) OSIM m-iPP samples along the TD direction. The numbers (in μm) on the left side represent the distance away from the sample surface. The flow direction is vertical.

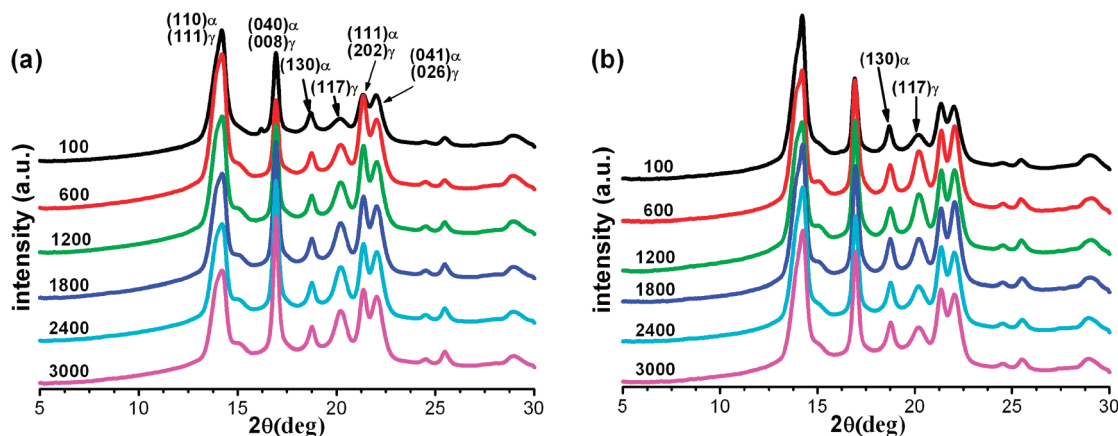


Figure 3. Plots of integrated WAXD intensity as a function of 2θ for (a) CIM and (b) OSIM samples. The intensity was calculated from the circulated integration of 2D WAXD pattern. The numbers on the left sides represent the distance away from the sample surface (μm). The $(130)_\alpha$ and $(117)_\gamma$ reflections at $2\theta = 18.6^\circ$ and 20.1° , respectively, typical of the α - and γ -crystal of iPP, are also indicated.

TABLE 1: Crystallinity Estimated at Different Depths of CIM and OSIM Samples

crystallinity	distance from skin					
	100 μm	600 μm	1200 μm	1800 μm	2400 μm	3000 μm
CIM	0.367	0.383	0.389	0.389	0.386	0.371
OSIM	0.416	0.443	0.398	0.402	0.415	0.408

from 2400 to 3000 μm . Generally, f_γ increases with increasing crystallization temperature and/or lowering cooling rate,^{8,12} which is consistent with the observation that the inner CIM sample exhibits a maximum amount of γ -crystal. For OSIM, f_γ (0.564) at 100 μm is basically the same as the CIM sample. Unexpectedly, f_γ first increases (0.69 at the depth of 600 and 1200 μm) and then decreases gradually, with the minimum f_γ (0.57) in the core (3000 μm). Upon molding of OSIM samples, continuous shearing is imposed on the melt before solidification, whereby the shear flow can cause further heating leading to slower cooling. Thus, the cooling rate should be lower in the inner layers of OSIM samples than that of CIM samples. It is natural to speculate that the inner layers of OSIM samples produce more γ -crystals than or at least equivalent to that of CIM samples. The presence of the minimum f_γ value (0.57) in the core of OSIM has important implications, in which another mechanism to control the γ -crystal formation under flow and thermal fields must take effect.

Figure 5 shows 2D SAXS patterns at different depths of CIM and OSIM samples. In the case of CIM samples, a visible and

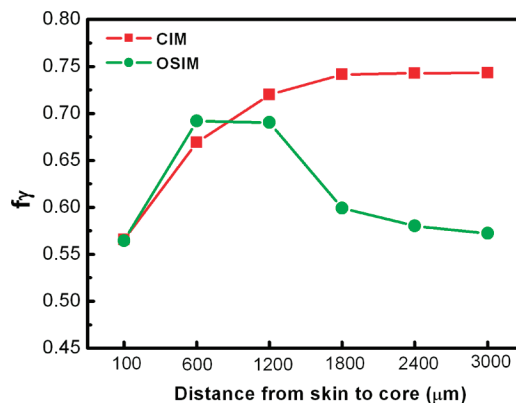


Figure 4. Fraction of γ -crystal, f_γ , evaluated from the X-ray diffraction profiles from skin to core of CIM and OSIM samples.

narrower meridional maximum is seen at the 100 μm position, while a very weak and broad meridional maximum appears in other positions. Meanwhile, the equatorial streak in 100 μm position is very obscure, and the equatorial streak in other positions is totally invisible. For OSIM samples, there are distinct scattering maxima along the flow direction at different positions, but like CIM samples, the equatorial streak of OSIM samples is not visible. It is generally accepted that the meridional maxima in the SAXS pattern can be attributed to the formation of the kebab-like lamellar structures that are spatially correlated and perpendicular to the flow direction, while the equatorial streak can be attributed to the formation of shish or mi-

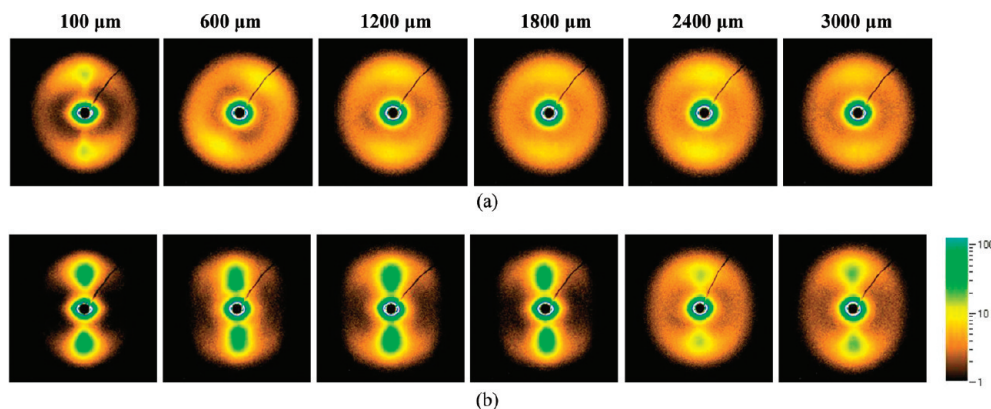


Figure 5. 2D SAXS images taken at different distances from the surface of m-iPP samples: (a) CIM and (b) OSIM. The numbers (in μm) on the left side represent the distance away from the sample surface. The flow direction is vertical. Those images were corrected by air scattering.

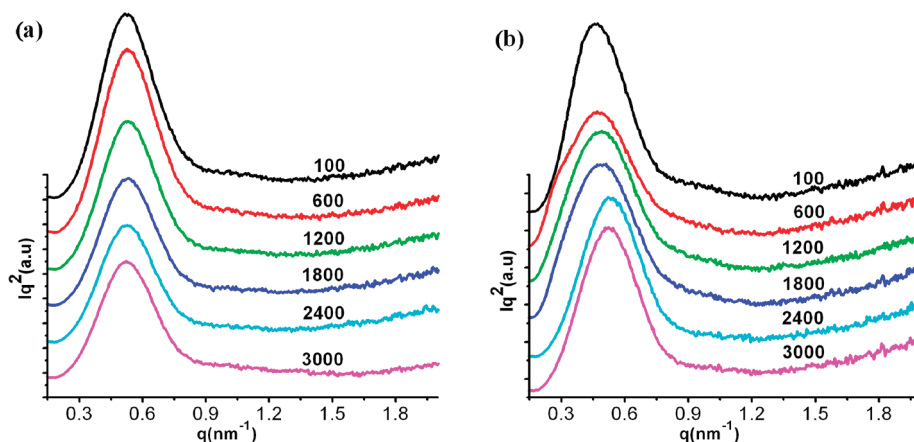


Figure 6. Lorentz-corrected SAXS intensity profiles at different distances from the surface: (a) CIM and (b) OSIM. The number (in μm) represents the distance away from the sample surface.

crofibrils,³⁵ and/or a^* -axis oriented “daughter” lamellae growing epitaxially.³⁶ Therefore, stacks of oriented crystalline lamellae or kebabs should exist in the 100 μm depth of CIM samples and across the whole depth of OSIM samples. The formation of shish-kebabs structure is due to orientation-induced crystallization. It is worth noting that the missing equatorial streak cannot be considered as the absence of the shish structure. According to the mechanism of shear-induced crystallization of polymer melts, if the linear row nuclei or shish do not form, the nucleation and growth of kebabs or lamellae perpendicular to the flow direction would be impossible.^{15,37,38} The possible reason of the invisible equatorial streak is that the size of isolated shish is too small or the concentration of shish is too low that SAXS cannot easily detect them. Toward the core region of CIM samples, the weak and broad meridional maximum implies less oriented arrangement of lamellae as a result of a low level of shear flow.

To probe the superstructure of m-iPP in the CIM and OSIM samples, Lorentz-corrected intensity profiles of circularly integrated 2D SAXS patterns of all of the samples at different depths are shown in Figure 6. It is seen that a dominant scattering maximum appears in all SAXS curves, typical of SAXS profiles for iPP. Using Bragg’s law, the long spacing (L) was estimated from the peak position, where the results are listed in Table 2.

For the CIM sample, the long period in the skin layer is slightly larger than that in the interior region, but it does not change considerably in the whole sample. In contrast, the OSIM sample exhibits a large long period almost at every depth of the sample as compared to CIM. This is consistent with our expectation that OSIM offers greater melt-shearing effects. The

difference of long periods of the samples is due to the shear-induced crystallization and the temperature of crystallization.

The crystal structure distribution can be indirectly verified by the DSC study of melting behavior of CIM and OSIM samples, where the results are shown in Figure 7. All thermograms of different samples taken at different depths exhibit double melting peaks (not a function of heating rate), which can be attributed to the coexistence of γ - and α -crystals as observed by WAXD (Figures 2 and 3). This has been well documented in the literature; when m-iPP samples isothermally crystallized from the melt, they generally show broad endotherms in the form of double melting.^{2,8} The broad low-temperature endotherm (120–145 $^{\circ}\text{C}$) represents the melting of γ -crystal, whose crystals always contain α/γ structural disorder, while the narrow endotherm (within 5 $^{\circ}\text{C}$) around 149 $^{\circ}\text{C}$ can be attributed to the melting of the more ordered α -crystals.

It is possible to evaluate f_{γ} from the relative area of the peaks in the DSC scans. The relative content of the γ -crystal with respect to the α -crystal can be estimated as follows:³⁹

$$f_{\gamma} = \frac{(\Delta H_{\text{m}}(\infty)_{\gamma}/(\Delta H_{\text{m}}^{\circ})_{\gamma})[\Delta H_{\text{m}}(\infty)_{\alpha}/(\Delta H_{\text{m}}^{\circ})_{\alpha} + \Delta H_{\text{m}}(\infty)_{\gamma}/(\Delta H_{\text{m}}^{\circ})_{\gamma}]}{(\Delta H_{\text{m}}(\infty)_{\gamma}/(\Delta H_{\text{m}}^{\circ})_{\gamma}) + (\Delta H_{\text{m}}(\infty)_{\alpha}/(\Delta H_{\text{m}}^{\circ})_{\alpha})} \quad (5)$$

where $\Delta H_{\text{m}}(\infty)_{\gamma}$ and $\Delta H_{\text{m}}(\infty)_{\alpha}$ represent the melting enthalpies of α - and γ -crystals that develop upon completion of crystallization (they can be measured from the area of each endotherm by deconvolution of DSC scan), and $(\Delta H_{\text{m}}^{\circ})_{\gamma}$ and $(\Delta H_{\text{m}}^{\circ})_{\alpha}$ are equilibrium melting enthalpies of γ - and α -crystals. The values

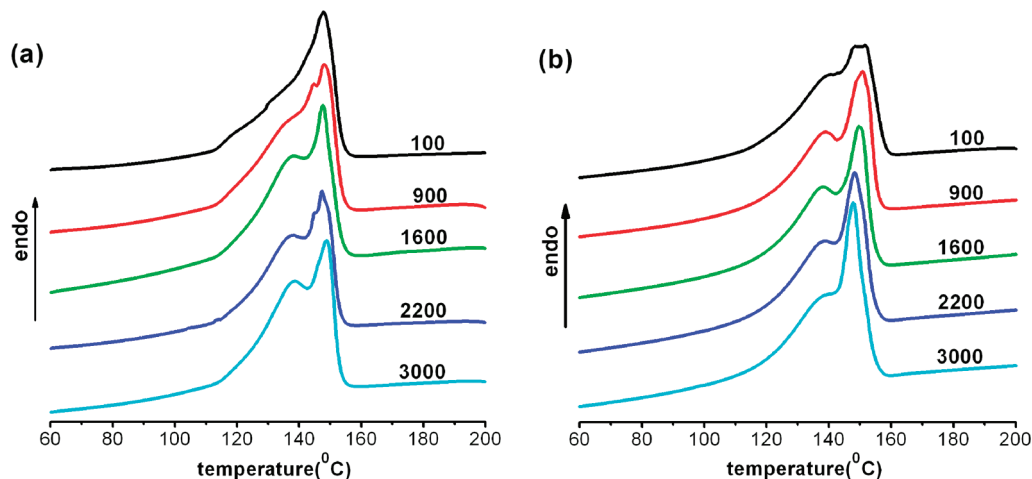


Figure 7. DSC curves of sample at different depths from the surface: (a) CIM and (b) OSIM. The numbers (in μm) represent the distance away from the sample surface.

TABLE 2: Long Spacing (L) at Different Depths of CIM and OSIM Samples

long spacing (nm)	distance from the skin					
	100 μm	600 μm	1200 μm	1800 μm	2400 μm	3000 μm
CIM	12.2	12.0	11.8	11.7	12.0	11.9
OSIM	13.6	13.4	12.8	12.7	12.0	12.0

TABLE 3: f_γ (DSC) at Different Depths of CIM and OSIM Samples

f_γ (DSC)	distance from skin				
	100 μm	900 μm	1600 μm	2200 μm	3000 μm
CIM	0.6680	0.7474	0.7711	0.7751	0.7899
OSIM	0.7085	0.7253	0.7403	0.7078	0.6896

of ΔH_m° for the α form were assumed to be 209.5 J/g,⁴⁰ whereas ΔH_m° for the γ -crystal was assumed to be 144.8 J/g.⁴¹ The calculated values of f_γ (DSC) are listed in Table 3. The DSC results are consistent with the WAXD results; that is, f_γ (DSC) increases gradually from skin to core in the CIM sample, while it first increases and then gradually decreases in the OSIM sample.

Molecular Orientation of CIM and OSIM Samples. Figure 8 shows the distribution of Hermans' orientation function through the depth of the samples. For the CIM sample, the molecular orientation at the 100 μm depth is as high as 0.96,

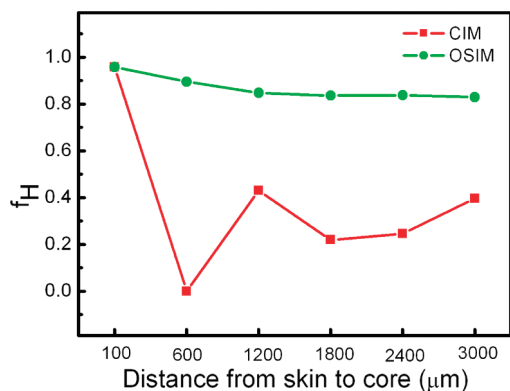


Figure 8. Degree of molecular orientation (f_H) calculated from the $2\theta = 17^\circ$ (040 and 008 reflections) from skin to core of CIM and OSIM samples.

but suddenly reduces to 0 at the 600 μm depth, and then slightly increases to 0.22–0.43 from 1800 μm to core (3000 μm). It is worth noting that the undetectable molecular orientation at 600 μm does not indicate completely random crystallites. In this case, the overall molecular orientation at $2\theta = 17^\circ$ represents the superposition of two kinds of crystals (α - and γ -crystals) orientation and cancellation of the diffraction from parents and daughters of α -crystal to the axis orientation.⁴² The morphology detected at 600 μm is due to the complex flow perturbations imposed by the combined effects of filling and packing stages. The morphological development would be involved in different arrangements of oriented lamellae (shish, kebabs, and daughter lamellae) relative to the reference (machine) axis, resulting in almost no azimuthal distribution (i.e., the apparent degree of orientation is 0). The broad meridional maximum SAXS pattern at the same position indicates that the crystalline lamellae maintain some molecular orientation (Figure 5). If more SAXS patterns were obtained at 600 μm , there must be different SAXS patterns that involve tilt to the left side patterns as well as the ones tilted to the right side. This is to say that the orientation of the lamellar at 600 μm is weak and not so unanimous as compared to that at 100 μm . For the OSIM sample, the molecular orientation is very high (0.83–0.96) through the depth of the sample as a result of the continuous shear during cooling, which only slightly decreases from skin to core.

The molecular orientation according to the azimuthal distribution at $2\theta = 17^\circ$ represents the overall molecular orientation of α - and γ -crystals. To separately evaluate the orientation of α - and γ -crystal, the azimuthal distribution of $(130)_\alpha$ at $2\theta = 18.6^\circ$ and $(117)_\gamma$ at $2\theta = 20.1^\circ$ was studied as follows, which corresponds to molecular orientation of α - and γ -crystals, respectively.

Figure 9 shows the azimuthal profiles of $(117)_\gamma$ at $2\theta = 20.1^\circ$. Interestingly, the azimuthal profile exhibits three peaks, which appear to be a common feature across the depth of OSIM samples. However, this feature is not seen in other positions of the CIM sample (only one broad hump appears in the azimuthal profile), only at the 100 μm depth. The three-peak azimuthal profile indicates the parallel chain axis orientation of γ -crystal,⁴³ which has previously been observed in commercial ZN-iPP samples prepared by shear-controlled orientation injection molding (SCORIM) technique⁴⁴ as well as on the surface of pitch-based carbon or Kevlar fiber-reinforced iPP composite fibers.⁴⁵

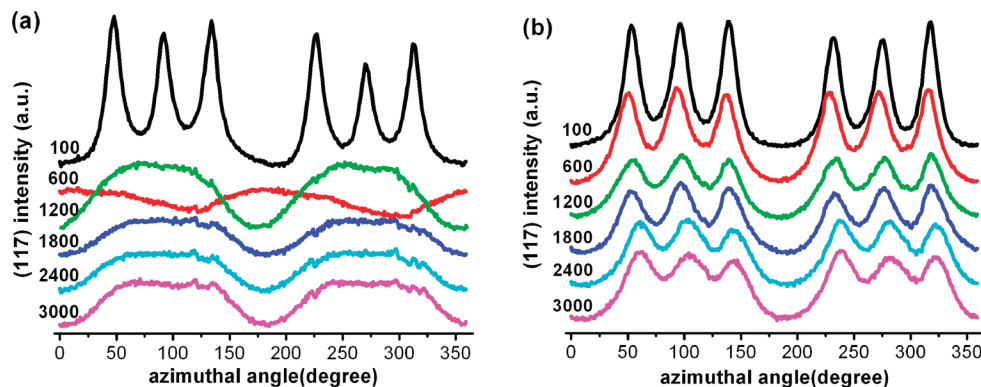


Figure 9. Azimuthal profiles $I(\varphi)$ taken at the $2\theta = 20.1^\circ$ $(117)_\gamma$ reflection as a function of azimuthal angle φ through the depth of sheared m-iPP samples with different shear modes: (a) CIM and (b) OSIM. The curves are marked with the distance from the skin (μm).

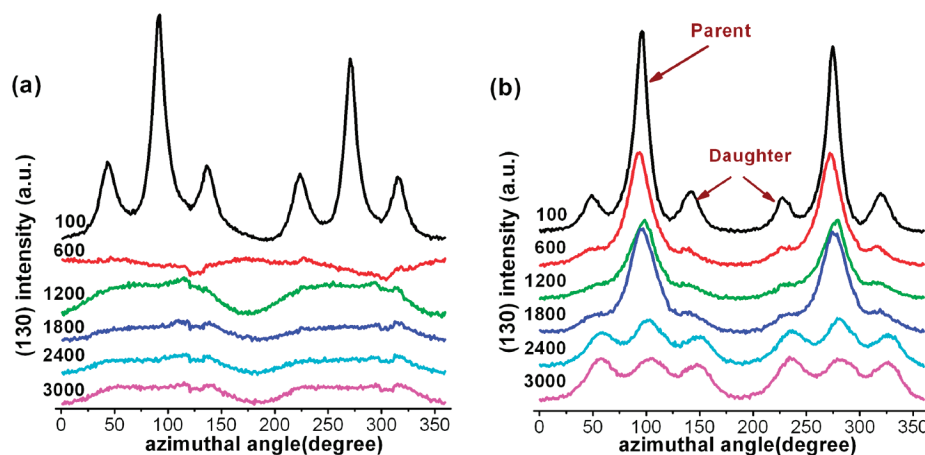


Figure 10. Azimuthal profiles $I(\varphi)$ taken at the $2\theta = 18.6^\circ$ $(130)_\alpha$ reflection as a function of azimuthal angle φ through the depth of sheared m-iPP samples with different shear modes: (a) CIM and (b) OSIM. The curves are marked with the distance from the skin (μm).

The parallel chain axis orientation relative to the reference axis is one of the two types of molecular orientation found in the γ -crystal (the two molecular orientations are parallel chain axis orientation and perpendicular chain axis orientation).^{46–48} The parallel chain axis orientation exhibits the characteristics with one-half of the chain axes parallel to the reference axis and the other half tilted at an angle of $\sim 81^\circ$ with respect to the reference axis. The X-ray fiber diffraction pattern for the parallel chain axis orientation can be characterized by the appearance of $(117)_\gamma$ both on the equator and on the first layer line. As a result, the three-peak azimuthal profile of the $(117)_\gamma$ diffraction is seen. The perpendicular chain axis orientation can be described as “cross- β ”, whose feature is the alignment of the c_γ -axis (that is the direction of stacking of bilayers of chains) parallel to the reference axis; that is, the two sets of chain axes are aligned along the directions nearly normal to the reference axis. In this scenario, the corresponding diffraction pattern can be characterized by the presence of a strong meridional spot at $2\theta = 17^\circ$, corresponding to the $(008)_\gamma$ reflection. The remaining reflections of the γ -form exhibit low intensity. According to the recapitulation of the results so far, re-examining 2D WAXD patterns in Figure 2, one can find that there is no diffraction at the meridional spot at $2\theta = 17^\circ$, and the three-peak azimuthal profile appears in the high molecular orientation area ($100 \mu\text{m}$ depth of CIM sample, the whole OSIM sample in Figure 9). Therefore, in the high molecular orientation area of injection molded parts, only parallel chain axis orientation of γ -form exists without perpendicular chain axis orientation.

For the OSIM sample, the parallel chain axis orientation of γ -crystal is obtained in the whole sample as a result of

continuous shear during melt solidification (Figure 9b). So far, the γ -crystal orientation is unable to explain the observation of nonmonotonic γ -crystal content from skin to core, especially the formation of minimum γ -crystal ($f_\gamma = 0.57$) at the $3000 \mu\text{m}$ depth (Figure 6). It is natural to suspect the underlying mechanism for the γ form formation may be closely related with the α -crystal. On the basis of recent reports by Cheng et al.,⁴⁹ a small-angle change of stem orientation of the α -form has a profound effect on the formation of γ -form in iPP due to the molecular epitaxy of the γ -form on the α -form. To this end, further characterization of the orientation distribution of α form is analyzed below.

Figure 10 shows the azimuthal profiles of $(130)_\alpha$ at $2\theta = 18.6^\circ$, representing the orientation distribution of α -crystal alone through the depth of CIM and OSIM samples. Similar to the behavior of the $(117)_\gamma$ reflection, three-peak azimuthal profiles of $(130)_\alpha$ also appear only at the $100 \mu\text{m}$ depth (but not the other depths) in the CIM sample as well as in the whole region of OSIM samples (Figure 10). To explain the reason of the special γ -crystal distribution in OSIM sample, we should distinguish the parent lamellae and the daughter lamellae first. The three-peak azimuthal profiles shown in Figure 10a and b indicate a shish-kebab structure containing lamellar branching in the α -crystal.²² This special structure results in a unique diffraction pattern. Considering the $(130)_\alpha$ reflection in this pattern, the diffraction from the parent lamellae appears on the equator, and that from the daughter lamellae on the first layer line. Such a structure would lead to the three-peak azimuthal profile for the $(130)_\alpha$ reflection when the molecular orientation is high, which is the case in Figure 10a and b. In these figures,

TABLE 4: Parent–Daughter Ratio $[R]$ at Different Depths of CIM and OSIM Samples

parent– daughter ratio $[R]$	distance from skin					
	100 μm	600 μm	1200 μm	1800 μm	2400 μm	3000 μm
CIM	3.897					
OSIM	4.051	4.534	5.886	3.792	1.573	1.383

the reflection peaks at ca. 45° and 135° are from the daughter lamellae, and that at ca. 90° is from the parent lamellae. In Figure 10b, from skin to core, except the $100\ \mu\text{m}$ azimuthal reflection, the relative intensity of the reflection from parent lamellae with respect to that from daughter lamellae is gradually reduced. Similar to the method suggested by Fujiyama,²⁸ who calculated the fraction of daughter lamellae using the $(110)_\alpha$ reflection, the ratio of parent lamellae to daughter lamellae ($[R]$) according to the $(130)_\alpha$ reflection can be estimated as follows:

$$[R] = \frac{2P}{D_1 + D_2} \quad (6)$$

where P is the area around the azimuthal angle of 90° , and D_1 and D_2 represent the areas around 45° and 135° in Figure 10, respectively, after the subtraction of baseline area. The data are reported in Table 4. In the core (i.e., $3000\ \mu\text{m}$ depth) of the OSIM sample, the parent–daughter ratio is the smallest ($[R] = 1.38$), which is in coincidence with the smallest f_γ (0.57). It is worth noting that the relative flat azimuthal patterns are formed at depths of 600 – $3000\ \mu\text{m}$ in the CIM sample, indicating approximately random orientation of the α -crystal in those areas, whereby $[R]$ could not be obtained.

Discussion

The results indicate interesting but distinctly different spatial crystalline structure distributions of γ -crystal in m-iPP samples obtained via two industrial processes: CIM and OSIM. The distinct difference comes from the different thermal and flow histories imposed by these two processing technologies. To understand the structure and processing relationship under the two conditions, we first consider the following scenario.

Injection molding of semicrystalline polymers is essentially a flow-induced nonisothermal crystallization process. Temperature field and shear field during injection molding will significantly influence the crystallization process and result in different crystal structure distribution.^{17,36} Generally, flow fields introduce different degrees of anisotropy into polymer melts, which accelerates crystallization kinetics and alters final morphology. It is well established that the orientation of polymer molecules is a result of the competition between shear-induced orientation and chain stretching and subsequent relaxation. The relaxation behavior is dependent on crystallization temperature or degree of supercooling under which different diffusion rate of chains and subsequent different ordering processing takes place.

We now look back to understand the two factual molding processes used in the present work and the spatial γ -crystal distribution observed in the molded samples. For CIM, a cooperative effect of flow field and temperature gradient can only preserve oriented morphology at the outer area of the sample (Figure 8), where f_γ monotonously increases from skin to core (Figure 4). For OSIM, the oriented morphology can be maintained throughout the whole region of sample (Figure 8),

where f_γ is a nonmonotonic change from skin to core and the minimum amount of γ -crystal occurs in the core region (Figure 4).

Figure 11 shows the proposed schemes for morphological evolution of m-iPP during CIM and OSIM processing. During CIM processing, the melt is first injected into the mold under elongational flow accompanied by fountain flow at the flow front (Figure 11a). When the melt fills the cavity of the mold, the hot iPP melt contacting with the cold walls solidifies by rapid crystallization and preserves the molecular orientation in the skin of the sample (Figure 11b). The skin layer of an injection molded bar is usually about tens of micrometers or more with a very high molecular orientation. Next to the skin, due to elongational flow and high cooling rate, the flow-induced oriented threadlike nuclei are maintained to a large extent and then subsequently form oriented crystals in the shish-kebab form.¹⁷ This area is designated as the shear region. When the mold filling stage is finished (Figure 11c), the flow front stops moving, and the shearing stress starts to decay. At the same time, the packing stage begins. The solidification process occurs progressively from the just frozen region to the core through cooling (Figure 11c–e). The lower cooling rate in the interior region allows a sufficient time for stretched chains to relax and consequently form spherulites with random crystal orientation. However, some residual molecular orientation cannot be ruled out due to the effect of the packing stage (e.g., as seen in 2D SAXS images of Figure 5, Figure 8), which consists of a slight melt flow that would reorient some oriented nuclei and induce corresponding oriented crystals.

In the case of CIM samples, the external region ($100\ \mu\text{m}$) maintains a high degree of molecular orientation where α -form crystals can be characterized by lamella-branched shish-kebab (Figure 9a), and γ -form crystals consist of parallel chain axis orientation (Figure 10a). Toward the core, there is no obvious orientation structure (Figures 9a and 10a). This changing structure is accompanied by the monotonously increase of f_γ , with the minimum f_γ (0.57) appearing at $100\ \mu\text{m}$ and the maximum f_γ (0.74) in the inner area (Figure 6). The crystallization in the core region is expected to take place mainly under quiescent conditions. The cooling rate is thus a governing factor for the formation of the γ -crystal, whereby it is understandable that the maximum γ -crystal is obtained in the core region.^{8,12}

In the OSIM process, the initial mold filling stage of iPP melt is the same as that of CIM (Figure 11a'). Similarly, the outer melt would contact the cold walls and undergo a fast cooling process forming the surface of the sample (Figure 11b'). When the mold filling stage is finished, the reciprocating shear is imposed on the iPP melt by two pistons that move reversibly with the same frequency, and hence the molecular chains in the melt are oriented and further stretched. The formation of the oriented crystals next to the skin is a consequence of oriented molecular chains under such a complicated flow field. An interesting point is that the molecules close to the solid (or just frozen layer)—liquid boundary always crystallize earlier than those in the interior ones because of the larger supercooling. When crystallization progressively occurs from the mold wall to the core, the oriented crystals can be gradually formed due to the continuous shear flow until the gate of the mold freezes (Figure 11b'–d'). At the same time, with the gradual reduction of the melt volume in the mold, the local pressure of the melt increases because the driving pistons are maintained at the same frequency. When the shear flow ceases after the gate freezes, the remaining melt crystallizes under static conditions, and the relaxation of oriented iPP molecules inevitably occurs as a result

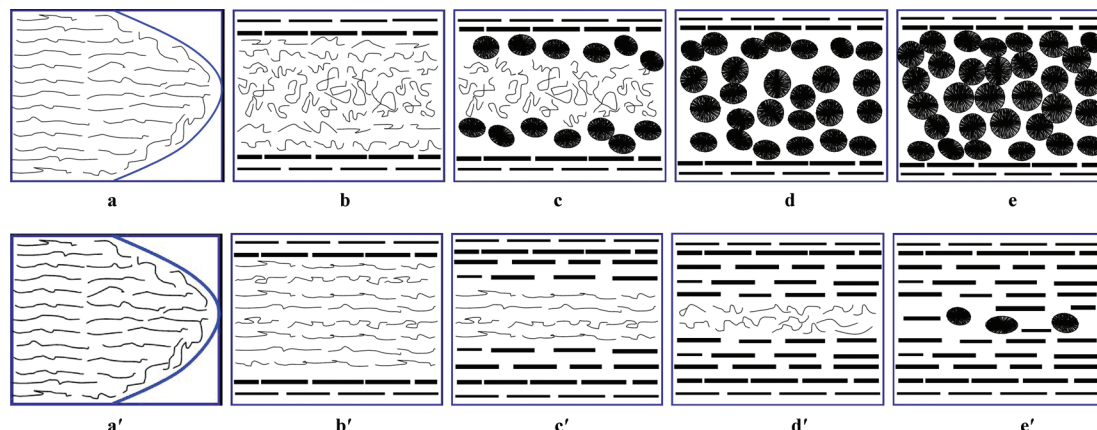


Figure 11. Schematic diagram representing the morphological evolution of CIM (a, b, c, d, e) and OSIM (a', b', c', d', e') samples.

of a lower cooling rate in the core region (Figure 11e'). Therefore, depending on the competition between the flow-induced orientation and subsequent relaxation processes of chain segments, different morphology (e.g., spherulites versus oriented shish-kebab crystals) can be formed. In our case, a higher degree of orientation could be achieved even in the core of the sample (Figures 8–10). In addition, the degree of molecular and lamellar orientation in the interior region (intermediate and core layers) is less than that in skin layer for OSIM sample (Figure 8, Figure 5), because it is less effective for the shear flow to induce chain orientation than elongational flow.⁵⁰

For the OSIM sample, the lamella-branched shish-kebabs are formed in the whole sample, corresponding to the formation of parallel chain axis orientation of γ -crystal (Figures 9b and 10b). Our interpretation of the formation of this orientation is as follows. In the injection molding process, extensional deformation and/or oscillatory shear force the molecular chains to align along the flow direction, so the melt is well oriented before crystallization. Soon afterward, this oriented melt crystallizes into oriented γ -crystal with the parallel chain axis orientation by reversing a small angle of chain segments and/or the extended chain conformation in oriented melt directly transform to α -crystals. At the same time, f_γ showed nonmonotonic variation from skin to core and the lowest fraction of γ -crystal (0.57) in the core layer. As shown in Figure 11b'–d', chains at the solid–liquid boundary always undergo a continuous shear, so the oriented segments can be easily frozen and crystallized, which will inevitably affect the formation of the nonparallel chain structure of γ -crystal. It has been speculated that the crystal–liquid interphase may play a significant role in the formation of γ -crystal.⁵¹ Therefore, unlike the core region in CIM samples where the thermodynamics driving force is dominant for γ -crystal formation, the γ -crystal distribution of OSIM samples must be closely related to the flow-induced molecular orientation. Without question, the crystallization process of the most external area (100 μm) is greatly affected by the elongational flow, which enables chain to stretch and favors the formation of α -crystal rather than γ -crystal.⁴³ As the melt is rapidly cooled at the 100 μm depth near the mold, it is logical to find the least amount of γ -crystal in this layer due to the combined effect of strong flow and fast cooling. This can also be applied to explain the finding of the least γ -crystal content at 100 μm depth of CIM samples. In the region from 600 to 3000 μm depth, which is mainly subjected to shear flow, f_γ first increases to ca. 0.69 at the depth of 600 and 1200 μm and then decreases gradually, with the minimum f_γ (0.57) at 3000 μm depth (Figure 5). These results can no longer be explained by the mechanism of thermodynamically favored

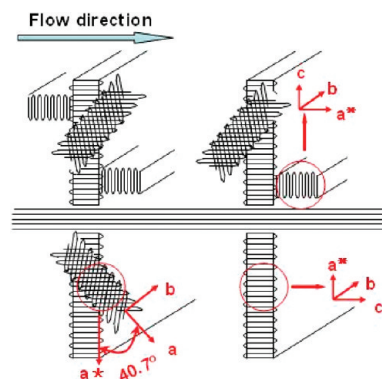


Figure 12. Model diagram of the structural relationship between α -crystal lamellae and γ -crystal lamellae (the morphology corresponding to the oriented area in Figure 11).

γ -crystal formation. Instead, it can be explained by the feature of epitaxy between γ - and α -crystals under the intense shear field of OSIM processing.

Figure 12 illustrates the schematic diagrams of epitaxy between γ - and α -crystals in the high molecular chain orientation region, that is, at 100 μm of CIM, or throughout of the whole OSIM sample (Figures 9 and 10), which incorporates the relationship between the parent and daughter of α -crystal lamellae and γ -crystal and the flow direction. In this model diagram, the lamella-branched shish-kebab is the same as demonstrated before,^{22,26–28} in which the parent lamellae with their c -axes preferentially aligned along the flow direction and the daughter lamellae with their a^* -axes parallel to the flow direction. The daughter lamellae are considered to grow epitaxially on the formed parent lamellae with an approximately $\pm 80^\circ$. The full details of epitaxial mechanism at the molecular level have been given in the literature.²⁶ Under flow, the stretched segments can crystallize into the shish structure, and the coil chains can subsequently crystallize into kebabs from the surface of the formed shish.⁴² Meanwhile, the γ -crystal can also grow on the initially formed α -crystal according to the online X-ray scattering experiments (the detailed results will be reported in the near future). Generally, the branching of both α - and γ -crystals from the α -crystal crystal is easy to occur as we know, while the α -crystal can also branch from the γ -crystal occasionally. However, the γ -crystal does not appear to be able to branch from the γ -crystal.^{11,25,52} As shown in Figure 12, the b -axis of the orthorhombic γ -crystal unit cell tilts by $\pm 40.7^\circ$ for γ -crystal lamellae connected to α -parent lamellae. We assume there is almost no γ -crystal lamellae connected directly to the shish and α -daughter lamellae based on the weak

diffraction at the equatorial direction of 2D SAXS (Figure 5). As a result, there are two distinguishable orientations of α -crystals (i.e., parent lamellae with c -axis orientation and daughter lamellae with a^* -axis orientation) with respect to the flow direction (Figure 9), and only one distinct orientation of the γ -crystal (i.e., parallel chain axis orientation) (Figure 10) in the high orientation area. This orientation pattern of the γ - and α -crystal has also been reported by Lotz and Wittmann from electron diffraction and microscopy studies.¹¹

The lowest f_γ value (0.57) in the core and relatively higher f_γ value (0.69) at 600 and 1200 μm depth of the OSIM sample (Figures 9b, 10b, and 12) can be explained as follows. As compared to the parent lamellae, the daughter lamellae are small and imperfect, and the size is not uniform. It is believed that the secondary nucleation ability of parent lamellae is much stronger than that of daughter lamellae. The core has the lowest parent–daughter ratio (1.38) (Table 4), which indicates the existence of fewer parent lamellae and less space for nucleation and growth of α -crystal daughter lamellae and γ -crystal lamellae. As compared to the core region, the parent–daughter ratio is higher in the external layers (600 and 1200 μm), offering more secondary nucleation sites for growth of the γ -crystals (Table 4).

In addition to secondary nucleation of parent lamellae, which favors the formation of γ -crystal, there are two other possible factors for promotion of γ -crystal at the 600 and 1200 μm depths of OSIM samples. The first factor involves the production of a relatively larger amount of row nuclei in the intermediate regions (e.g., 600 and 1200 μm) of OSIM, as indicated by the relatively stronger equatorial streak in SAXS (Figure 5). In this case, the large concentration of crystallizable sequences would result in a great deal of defects during crystallization and favor the formation of γ -crystal.³⁰ The second factor involves the possible higher local pressure in this region, which also favors the formation of γ -crystals.¹³

Conclusions

The spatial distribution of crystalline structures of m-iPP via CIM and OSIM was investigated in detail. The results can be summarized as follows:

The crystallinity at different depths of the OSIM sample is always higher than that of the CIM sample. The increased crystallinity can be attributed to the higher level of continuous shear.

The combined flow and temperature fields in two processes lead to different oriented crystalline structures distribution. The structures that contain shish-kebab and parallel chain axis orientation of γ -crystal appear at the high molecular orientation area, 100 μm of the CIM sample and the whole region of the OSIM sample. In the inner area of CIM samples, the lower flow-strain history and slower cooling produce almost random crystal orientation.

Both CIM and OSIM samples exhibit a mixture of α - and γ -crystal forms. From skin to core, f_γ raises monotonously in the CIM samples, which is mainly due to the thermodynamically favored formation of γ -crystal. In the OSIM samples, f_γ raises nonmonotonically from skin to core, where the thermodynamic factor does not play a dominant role to promote the γ -crystal crystallization. The special nonmonotonic γ -crystal distribution in the OSIM samples can be interpreted with a model of epitaxy between the oriented γ - and α -crystals. In this model, the parent lamellae provide secondary nucleation sites for daughter lamellae and γ -crystal, and the different content of parent lamellae results in variation of γ -crystal. The smallest parent–daughter

ratio $[R]$ (1.38) in the core results in the lowest fraction of γ -crystal (0.57); the relatively higher γ -crystal content (0.69) at 600 and 1200 μm depth (corresponding to $[R]$ of 4.5 and 5.8, respectively) can be attributed to the large amount of parent lamellae providing more nucleation sites for crystallization of γ -crystal. On the other hand, the higher local pressure and larger size of row nuclei provide the favorable conditions for the formation of γ -crystal at 600 and 1200 μm depth of OSIM samples.

The double melting peaks in DSC originated from the melting of γ - and α -crystal of m-iPP samples. The f_γ distribution calculated from the relative areas of the peaks in the DSC scans is consistent with the WAXD results.

In summary, the γ -crystal spatial distribution of m-iPP, which is formed under intense flow and thermal fields two polymer processes, has been studied. The effect of thermodynamic factor does not play a dominant role in γ -crystal crystallization under strong shear field, and the epitaxy between oriented γ -crystal and α -crystal provides a reasonable interpretation for the spatial distribution of γ -crystals in m-iPP. The parent lamellae of α -crystal provide the secondary nucleation sites for daughter lamellae and γ -crystal, and the different content of parent lamellae results in variation of γ -crystal.

Acknowledgment. We are indebted to Prof. Guo-Qiang Pan and Mr. Xiang-Cun Chen from the National Synchrotron Radiation Laboratory (China) for synchrotron WAXD measurements, and Dr. Lixia Rong and Jie Zhu from the Synchrotron Light Source, Brookhaven National Laboratory (U.S.), for their help with SAXS measurements. The Chinese team is thankful for financial support by the National Outstanding Youth Foundation of China (Grant No. 50925311) and the Opening Project of the State Key Laboratory of Polymer Materials Engineering (Sichuan University) (Grant No. KF201001), and the U.S. team is thankful for financial support by the National Science Foundation of the U.S. (DMR-0906512).

References and Notes

- (1) Brückner, S.; Meille, S. V.; Petraccone, V.; Pirozzi, B. *Prog. Polym. Sci.* **1991**, *16*, 361.
- (2) Alamo, R. G.; Kim, M. H.; Galante, M. J.; Isasi, J. R.; Mandelkern, L. *Macromolecules* **1999**, *32*, 4050.
- (3) VanderHart, D. L.; Alamo, R. G.; Nyden, M. R.; Kim, M. H.; Mandelkern, L. *Macromolecules* **2000**, *33*, 6078.
- (4) Alamo, R. G.; VanderHart, D. L.; Nyden, M. R.; Mandelkern, L. *Macromolecules* **2000**, *33*, 6094.
- (5) Thomann, R.; Wang, C.; Kressler, J.; Mulhaupt, R. *Macromolecules* **1996**, *29*, 8425.
- (6) Thomann, R.; Semke, H.; Maier, R. D.; Thomann, Y.; Scherble, J.; Mulhaupt, R.; Kressler, J. *Polymer* **2001**, *42*, 4597.
- (7) (a) De Rosa, C.; Auriemma, F.; Circelli, T.; Longo, P.; Boccia, A. C. *Macromolecules* **2003**, *36*, 3465. (b) De Rosa, C.; Auriemma, F.; Spera, C.; Talarico, G.; Gahleitner, M. *Polymer* **2004**, *45*, 5875.
- (8) (a) De Rosa, C.; Auriemma, F.; Circelli, T.; Waymouth, R. M. *Macromolecules* **2002**, *35*, 3622. (b) Auriemma, F.; De Rosa, C. *Macromolecules* **2002**, *35*, 9057. (c) De Rosa, C.; Auriemma, F.; Spera, C.; Talarico, G.; Tarallo, O. *Macromolecules* **2004**, *37*, 1441.
- (9) Brückner, S.; Meille, S. V. *Nature* **1989**, *340*, 455.
- (10) Meille, S. V.; Brückner, S.; Porzio, W. *Macromolecules* **1990**, *23*, 4114.
- (11) Lotz, B.; Graff, S.; Straupé, S.; Wittmann, J. C. *Polymer* **1991**, *32*, 2902.
- (12) Foresta, T.; Piccarolo, S.; Goldbeck-Wood, G. *Polymer* **2001**, *42*, 1167.
- (13) Campbell, R. A.; Phillips, P. J.; Lin, J. S. *Polymer* **1993**, *34*, 4809.
- (14) (a) Somani, R. H.; Hsiao, B. S.; Nogales, A.; Fruitwala, H.; Srinivas, S.; Tsou, A. H. *Macromolecules* **2001**, *34*, 5902. (b) Somani, R. H.; Yang, L.; Hsiao, B. S.; Agarwal, P. K.; Fruitwala, H. A.; Tsou, A. H. *Macromolecules* **2002**, *35*, 9096. (c) Hsiao, B. S.; Yang, L.; Somani, R. H.; Avila-Orta, C. A.; Zhu, L. *Phys. Rev. Lett.* **2005**, *94*, 117802.
- (15) Kumaraswamy, G.; Issaian, A. M.; Kornfeld, J. A. *Macromolecules* **1999**, *32*, 7537.

- (16) Li, L. B.; de Jeu, W. H. *Macromolecules* **2003**, *36*, 4862.
- (17) Zhu, P. W.; Edward, G. *Macromolecules* **2004**, *37*, 2658.
- (18) Gutierrez, M. C. G.; Alfonso, G. C.; Riekel, C.; Azzurri, F. *Macromolecules* **2004**, *37*, 478.
- (19) Kimata, S.; Sakurai, T.; Nozue, Y.; Kasahara, T.; Yamaguchi, N.; Karino, T.; Shibayama, M.; Korneld, J. A. *Science* **2007**, *316*, 1014.
- (20) Janeschitz-Kriegl, H.; Eder, G. *J. Macromol. Sci., Phys.* **2007**, *46*, 591.
- (21) Kalay, G.; Bevis, M. J. *J. Polym. Sci., Part B: Polym. Phys.* **1997**, *35*, 241.
- (22) Schrauwen, B. A. G.; Breemen, L. C. A. V.; Spoelstra, A. B.; Govaert, L. E.; Peters, G. W. M.; Meijer, H. E. H. *Macromolecules* **2004**, *37*, 8618.
- (23) Keller, A.; Kolnaar, H. W. *Mater. Sci. Technol.* **1997**, *18*, 189.
- (24) Wunderlich, B. *Macromolecular Physics*; Academic: New York, 1973; Vol. 2.
- (25) Lotz, B.; Wittmann, J. C.; Lovinger, A. J. *Polymer* **1996**, *37*, 4979.
- (26) Lotz, B.; Wittmann, J. C. *J. Polym. Sci., Part B: Polym. Phys.* **1986**, *24*, 1541.
- (27) Clark, E. S.; Spruiell, J. E. *Polym. Eng. Sci.* **1976**, *16*, 176.
- (28) Fujiyama, M.; Wakino, T.; Kawasaki, Y. *J. Apply. Polym. Sci.* **1988**, *35*, 129.
- (29) Agarwal, P. K.; Somani, R. H.; Weng, W.; Mehta, A.; Yang, L.; Ran, S.; Liu, L.; Hsiao, B. S. *Macromolecules* **2003**, *36*, 5226.
- (30) Hong, S. M.; Seo, Y. *J. Phys. Chem. B* **2007**, *111*, 3571.
- (31) Chen, Y. H.; Zhong, G. J.; Wang, Y.; Li, Z. M.; Li, L. B. *Macromolecules* **2009**, *42*, 4343.
- (32) Picken, S. J.; Aerts, J.; Visser, R.; Northolt, M. G. *Macromolecules* **1990**, *23*, 3849.
- (33) Natta, G.; Corradini, P. *Nuovo Cimento Suppl.* **1960**, *15*, 40.
- (34) Turner-Jones, A.; Aizlewood, J. M.; Beckett, D. R. *Makromol. Chem.* **1964**, *75*, 134.
- (35) Schultz, J. M.; Hsiao, B. S.; Samon, J. M. *Polymer* **2000**, *41*, 8887.
- (36) Zhu, P. W.; Edward, G. *Polymer* **2004**, *45*, 2603.
- (37) Eder, G.; Janeschitz-Kriegl, H.; Liedauer, S. *Prog. Polym. Sci.* **1990**, *15*, 629.
- (38) Somani, R. H.; Hsiao, B. S.; Nogales, A.; Srinivas, S.; Tsou, A. H.; Sics, I.; Balta-Calleja, F.; Ezquerro, T. A. *Macromolecules* **2000**, *33*, 9385.
- (39) De Rosa, C.; Auriemma, F.; Resconi, L. *Macromolecules* **2005**, *38*, 10080.
- (40) Cheng, S. Z. D.; Janimak, J. J.; Zhang, A.; Cheng, H. N. *Macromolecules* **1990**, *23*, 298.
- (41) Mezghani, K.; Phillips, P. J. *Polymer* **1998**, *39*, 3735.
- (42) Zhu, P. W.; Edward, G. *J. Mater. Sci.* **2008**, *43*, 6459.
- (43) Auriemma, F.; De Rosa, C.; Boscato, T.; Corradini, P. *Macromolecules* **2001**, *34*, 4815.
- (44) Kalay, G.; Bevis, M. J. *J. Polym. Sci., Part B: Polym. Phys.* **1997**, *35*, 241.
- (45) Dean, D. M.; Register, R. A. *J. Polym. Sci., Part B: Polym. Phys.* **1998**, *36*, 2821.
- (46) De Rosa, C.; Auriemma, F.; Perretta, C. *Macromolecules* **2004**, *37*, 6843.
- (47) De Rosa, C.; Auriemma, F.; De Lucia, G.; Resconi, L. *Polymer* **2005**, *46*, 9461.
- (48) Auriemma, F.; De Rosa, C. *Macromolecules* **2006**, *39*, 7635.
- (49) Cao, Y.; Van Horn, R. M.; Tsai, C. C.; Graham, M. J.; Jeong, K. U.; Wang, B.; Auriemma, F.; De Rosa, C.; Lotz, B.; Cheng, S. Z. D. *Macromolecules* **2009**, *42*, 4758.
- (50) Smith, D. E.; Babcock, H. P.; Chu, S. *Science* **1999**, *283*, 1724.
- (51) Meille, S. V.; Ferro, D. R.; Brückner, S. *Macromol. Symp.* **1995**, *89*, 499.
- (52) (a) Lotz, B.; Graff, S.; Wittmann, J. C. *J. Polym. Sci., Part B: Polym. Phys.* **1986**, *24*, 2017. (b) Stocker, A.; Magonov, S. N.; Cantow, H. J.; Wittmann, J. C.; Lotz, B. *Macromolecules* **1993**, *26*, 5915.

JP1002484